

Appendix C: Additional Information on Measurements of $\Delta g(x)$

Inclusive results

The inclusive π^0 results from PHENIX are already published [1], and those for inclusive jets from STAR have been accepted for publication[2]. Both experiments have released preliminary results from 2006 [3,4]. Data from both years are shown below in Figs. 1 and 2. The experiments have typically plotted curves for A_{LL} calculated at NLO [5,6] using the GRSV [7] polarized parton distribution functions (PDFs). The GRSV-std curve is based on the best fit to DIS data at the time of the analysis. GRSV $\Delta g = g$ and $\Delta g = -g$ refer to distributions where the gluons are maximally polarized at the input scale, either parallel to the proton, or anti-parallel. Such solutions were strongly disfavored by the first RHIC measurements in 2003 and 2004 and clearly rejected with the current data sets. The “GS- C” set [8] of PDFs has recently been reconsidered, as it has a small contribution to ΔG in the region of current sensitivity in the RHIC measurements, but a large total overall gluon spin contribution resulting primarily from low momentum fractions x . This behavior results in part from a node of Δg vs. x and is a feature that has arisen in a number of more recent analyses of polarized PDFs.

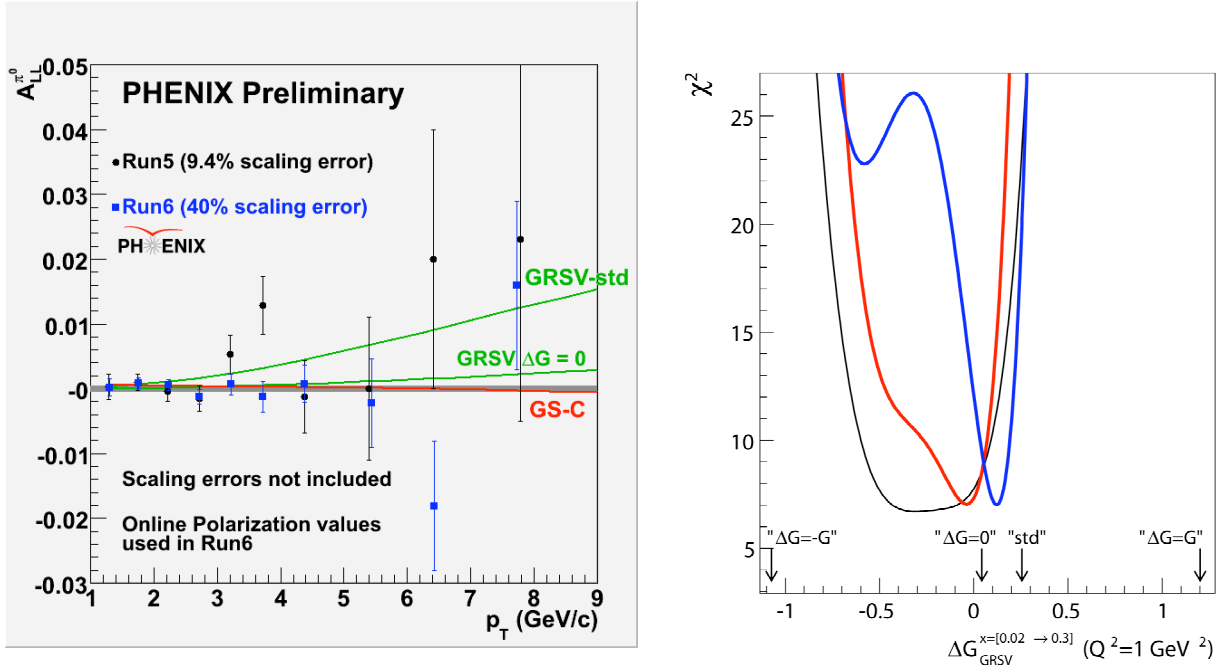


Figure 1. (left) Phenix inclusive- π^0 double spin asymmetry A_{LL} from 2005[1] and 2006[3]. The NLO theory curves are based on the GRSV[7] and GS-C [8] PDFs. (right) Plotted is the χ^2 derived by comparing the measurement to a range of solutions provided by GRSV, for which the value of the integral ΔG was constrained and the lepton scattering data refit. The horizontal axis is the contribution to the integral ΔG over the range $0.02 < x < 0.3$ in momentum fraction, to which the measurement is sensitive. The black curve is for the 2006 data, and the red and blue curves are for 25 pb^{-1} additional simulated data, under two different assumptions for the A_{LL} in the simulated data.

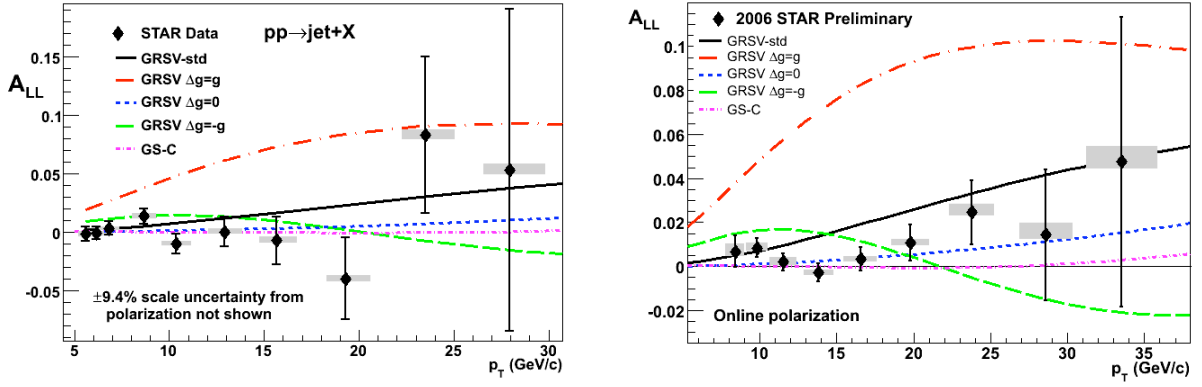


Figure 2. Inclusive-jet double spin asymmetries A_{LL} from STAR for 2005[2] (left) and 2006[4] (right). Curves shown are for four different PDF sets from GRSV[7] and for GS-C [8].

Both experiments have done statistical analyses to better understand the constraints the data place on ΔG . These have been based on a range of PDFs provided by GRSV where the integral value ΔG was fixed to different values covering the full range spanned between GRSV $\Delta g = g$ and $\Delta g = -g$, while allowing other parameters to adjust to provide the best possible fit to the DIS data. These PDF sets were used to calculate A_{LL} and compared to the data. PHENIX has done this by calculating χ^2 for the data vs. the range of PDFs, as represented by the black curve in Fig. 1. STAR has chosen to do its comparison by calculating confidence levels for each of the PDFs as compared to the STAR data, as shown in Fig. 3. The constraints from the two experiments have been combined into one χ^2 plot, as shown in Fig. 4. Both experiments provide some constraints on negative values of ΔG and strong constraints on how large ΔG can be in the region of sensitivity, $0.02 < x < 0.3$, and are inconsistent with GRSV-std.

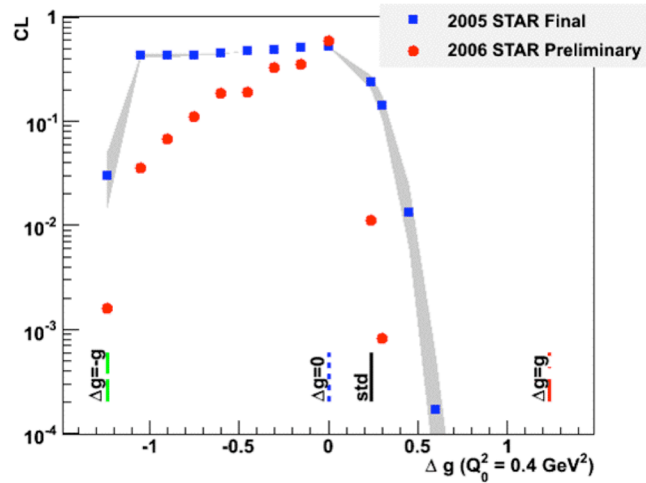


Figure 3. Confidence levels against STAR data for a set of PDFs provided by GRSV. The confidence level of each PDF is plotted at the ΔG (at the input scale) of that PDF.

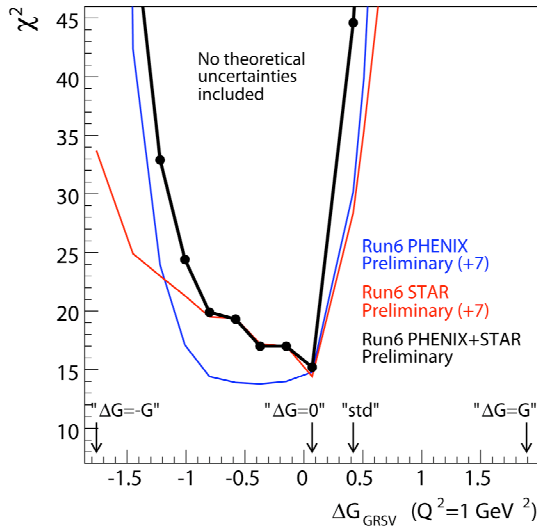


Figure 4. Joint χ^2 for the 2006 STAR and PHENIX 2006. The χ^2 for each experiment's data set was evaluated vs. A_{LL} , calculated for the range of GRSV PDFs, and then summed.

The question arises of how the many other sets of PDFs presented in the literature that have been fit to DIS data compare to the RHIC data. The $\Delta g(x)$ of a large number of older and more recent PDFs are shown in Fig. 5, plotted at a scale of 10 GeV^2 . The four curves drawn with heavy lines are the GRSV PDFs used for Figs. 1 and 2. STAR has recently gained the capability of calculating the single-jet A_{LL} for these PDFs in the same framework as the GRSV PDFs, and used those to do a confidence level plot based on the 2005 data. This is shown in Fig. 6. The PDFs that continue to have reasonably large confidence levels in light of the data have in common that they give relatively small contributions to ΔG in the region of x addressed so far at RHIC. They have either small and positive ΔG , moderately small negative ΔG , and/or nodes.

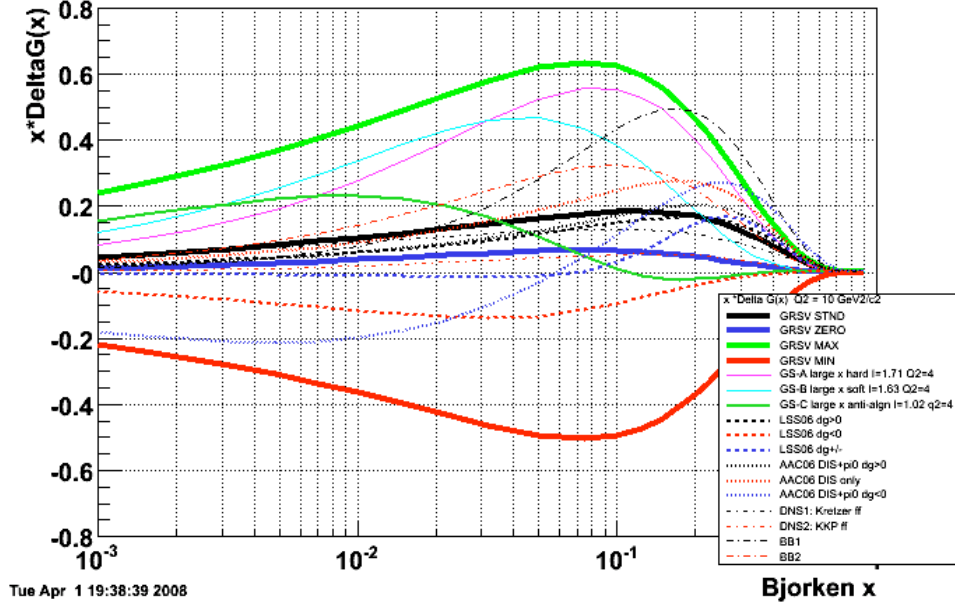


Figure 5. The gluon distribution functions at $Q^2=10 \text{ GeV}^2$ of a wide range of recent fits to DIS data. The four bold lines are the GRSV PDFs used in Figs. 1 and 2. GRSV[7], GS[8], LSS[9], AAC[10], DNS[11], BB[12].

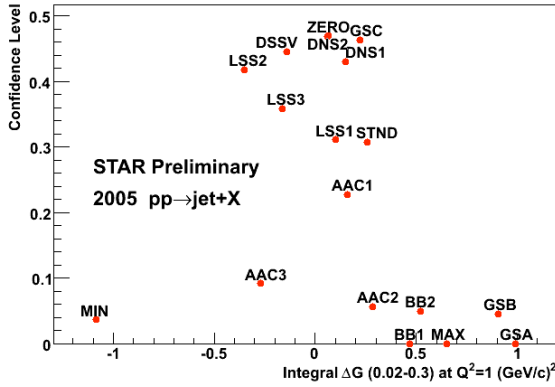


Figure 6. Confidence levels based on a comparison of A_{LL} calculated for many PDFs to the STAR inclusive jet data from 2005. The designations MIN, ZERO, MAX and STD refer to GRSV[7]. The full key to references is in Fig. 5.

As described in the main report, the RHIC data have now been included in a global NLO analysis [13] on equal footing with DIS and SIDIS data. Figure 7 shows $\Delta g(x)$ and the anti-quark distributions found in this analysis. The central region of RHIC sensitivity, $0.05 < x < 0.2$, is indicated on the plot. It is clear that previous fits such as GRSV-std and DNS are no longer supported by the data. The best fit has a node in the RHIC range, and it is clear that the error band expands considerably at lower x . The presence of nodes as in this fit and GS-C directs our attention to gaining sensitivity to the functional form of $\Delta g(x)$. Figure 8 shows distributions of gluon momentum fraction x for two p_T bins for

inclusive jets at STAR. Low p_T bins integrate over a wide range in x , and high p_T bins focus on a region higher in x , providing a somewhat crude map of the x dependence. The higher statistics achievable in the next run will be necessary to take full advantage of this aspect of the inclusive data.

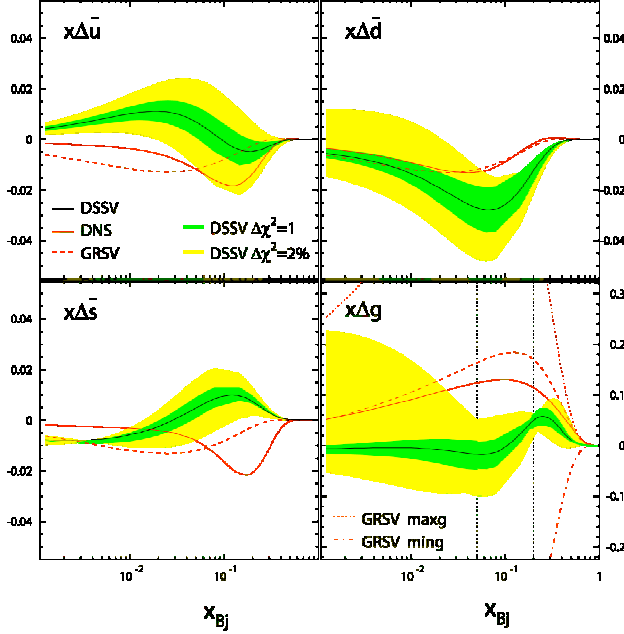


Figure 7. PDFs for gluons and anti-quarks as determined from a global NLO fit[13] to the RHIC inclusive π^0 and jet data on the same footing as DIS and SIDIS data. Shown are $\chi^2=1$ and 2% bands representing the uncertainty in these distributions. The central x range of current RHIC sensitivity is inside the vertical lines in the lower right plot for $\Delta g(x)$.

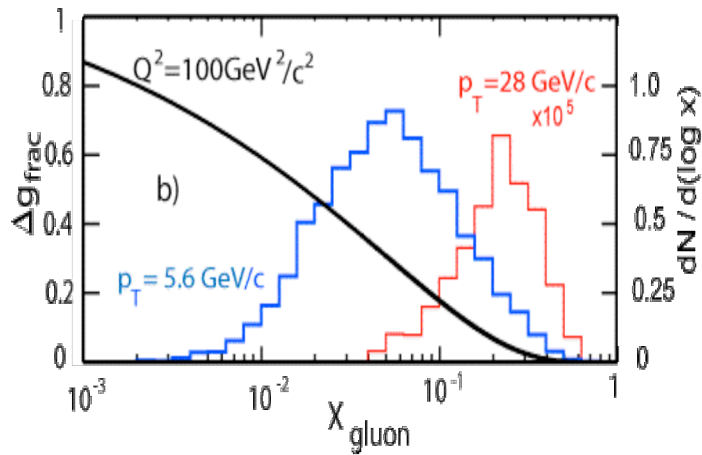


Figure 8. Distributions in gluon momentum fraction x for two experimental p_T bins for inclusive jets at STAR. These are generated from PYTHIA and thus do not include full NLO effects. In addition, a curve is shown for the fractional integral of Δg from x to 1 for GRSV-std.

Di-jet correlations

Two-body final states such as di-jets and gamma-jets can be used to gain sensitivity to the shape of $\Delta g(x)$. This is straightforward in LO, as shown by the relationships between detected kinematic observables and the partonic kinematic variables in Fig. 9. While these relationships no longer hold in NLO, they are often reasonable approximations and provide guidance as to what can be learned from such measurements. In LO, the measured A_{LL} can be related to the polarization of the two partons and the partonic analyzing power, a_{LL} , which is a function of the scattering angle. For di-jets there are three generic types of contributions, gg, qg and qq scattering. When the qg term dominates, it is rather straightforward to estimate the precision of $\Delta g(x)/g(x)$ implied by the uncertainty in the measurement of A_{LL} , as was done for a few points in the main document. The polarization of the quarks is known to some degree from the DIS measurements. Extracting $\cos(\theta^*)$ from the jet pseudo-rapidities, where θ^* is the partonic center-of-mass scattering angle, determines a_{LL} .

$$\begin{aligned}
 x_1 &= \frac{p_T}{\sqrt{s}} (e^{\eta_3} + e^{\eta_4}) \\
 x_2 &= \frac{p_T}{\sqrt{s}} (e^{-\eta_3} + e^{-\eta_4}) \\
 M &= \sqrt{x_1 x_2 s} \\
 y &= \frac{1}{2} \ln \frac{x_1}{x_2} = \frac{\eta_3 + \eta_4}{2} \\
 |\cos \theta^*| &= \tanh \frac{|\eta_3 - \eta_4|}{2}
 \end{aligned}$$

Figure 9. Relationships between observed final state kinematic observables and initial parton kinematical variables for LO two-body collinear kinematics. The quantities $x_{1,2}$ are the partonic momentum fractions, M is the invariant pair mass of the dijets, and θ^* the partonic center-of-mass scattering angle. The quantities $p_{3,4}$ and $\eta_{3,4}$ represent the transverse momenta and pseudo-rapidities of the jets, respectively.

Di-jet data from STAR for the 2005 run are shown in Fig. 10 in comparison to PYTHIA. There is good agreement between the data and the simulations. Experimental yields from 2006 were scaled to 50 pb^{-1} luminosity for the estimates of di-jet yields in the main document. Included in the estimates are realistic trigger thresholds, dead times, and limits imposed by systematic errors. Important for the future runs at STAR is the low

dead time expected with the upgrade to data acquisition known as DAQ1000. This should allow dead times $<10\%$ up to data rates of 1 kHz, and necessary rates are considerably less than that although more than the previous limit of $\sim 100\text{Hz}$. One sector of DAQ1000 was run successfully and routinely in 2008, and the installation of the rest of the electronics will be complete for the next run.

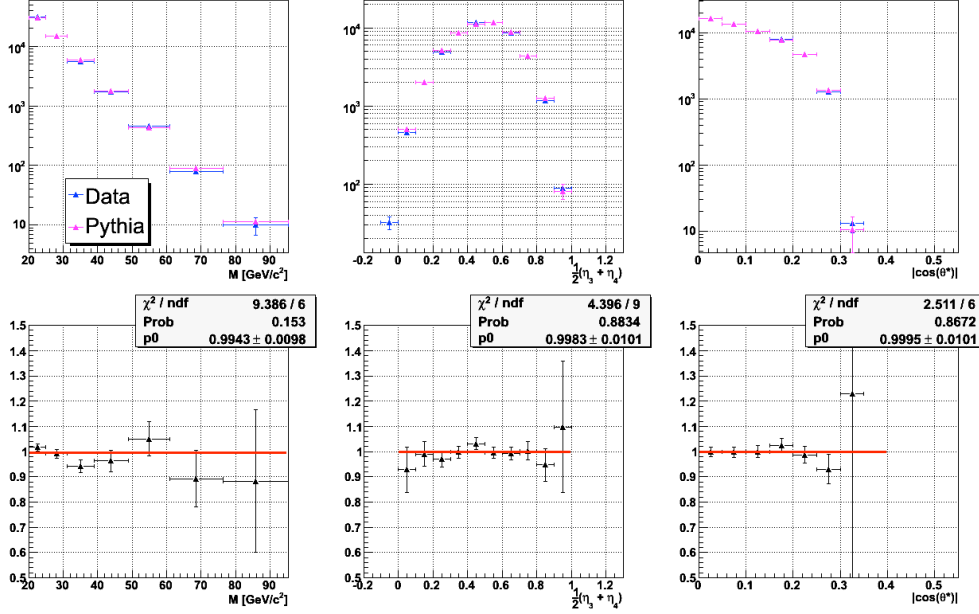


Figure 10. Di-jet yields in the STAR 2005 data. The yields are plotted vs. kinematic variables calculated from the jet pseudo-rapidities and transverse momenta, as described by the relationships given in Fig. 9. These are compared to PYTHIA simulations, and the ratio of data/PYTHIA is shown in the bottom row.

Mid-rapidity gamma-jet correlations

Analysis of gamma-jet events from the 2006 data set from STAR is currently being heavily pursued to understand the purity and efficiency with which the signal can be extracted from the dominating inclusive hadronic background. Note that this “background” is primarily the signal for our di-jet analysis. The efforts so far have, for the most part, focused on the endcap calorimeter region $1 < \eta < 2$ where leading order kinematic relationships give a better approximation to assigning the extracted x value properly to the quark and gluon. The studies are now making use of full PYTHIA/GEANT simulations with a detailed material model of STAR with significant samples of QCD background and direct photons events.

The starting inclusive distributions at $p_T \sim 10$ GeV have a 1:10 ratio of direct photons to π^0 s. Charged pions can also make significant energy deposition in the calorimeter but this is typically less than π^0 their energy suppressing them in the analysis relative to the neutral pions. The backgrounds rise rapidly with falling p_T and one goal is to push the analysis to $p_T < 10$ GeV to gain statistics. Important cuts on reducing the backgrounds are coincidence with the away-side jet, a requirement that the gamma candidate dominate the energy deposition in an isolation cone around it and finally a shower shape analysis in a shower maximum detector installed in the calorimeters specifically for this purpose. In addition there are many more detailed detector cuts that can be applied.

Figures 11 and 12 show three data sets. Actual data selected from the longitudinal portion of the 2006 run are shown in black. Monte Carlo (PYTHIA) data generated as QCD hard-scattering processes, primarily di-jets, processed through the full STAR detector model via GEANT are in green. Red histograms are Monte Carlo data generated with the direct photon processes from PYTHIA, again processed through full STAR simulations. In both figures the Monte Carlo curves have been normalized to the same integrated luminosity as was sampled for the data shown.

Candidate photon-jet events are selected from two jet events from a jet finder. They are checked to be back to back in azimuthal angle ϕ . Any jet in the endcap with a neutral fraction (p_T in 3×3 calorimeter tower cluster/ p_T of jets, plus tracks in an η - ϕ radius of 0.7) > 0.9 , is labeled a photon candidate and plotted in Figure 11. The endcap calorimeter has independent preshower signals from the front two layers of scintillator. The first is before the 1st lead layer the 2nd after it. The different panels represent different preshower detector conditions and indicate the point of conversion. In the upper-left panel the data are vetoed by a signal in the first two preshower layers thus selecting conversion after the 1st layer of lead. Due to the fact that a π^0 has two chances to convert, this provides a large suppression of π^0 backgrounds and provides a special but statistically limited sample for analysis. The upper-right panel of Fig. 11 is for a veto by the scintillator layer preceding the first Pb layer of the calorimeter and selects events that have not begun to shower prior to the calorimeter. The lower-right panel shows accepted

events that have signals in both preshower layers, i.e. that have begun to shower upstream of the calorimeter. Due to a large amount of material in the TPC end wheel and also tracking detectors near the beam, this sample contains the largest number of candidates. The main conclusion is that above threshold turn-on, $p_T > 6-7$ GeV/c, there is excellent agreement between the various histograms.

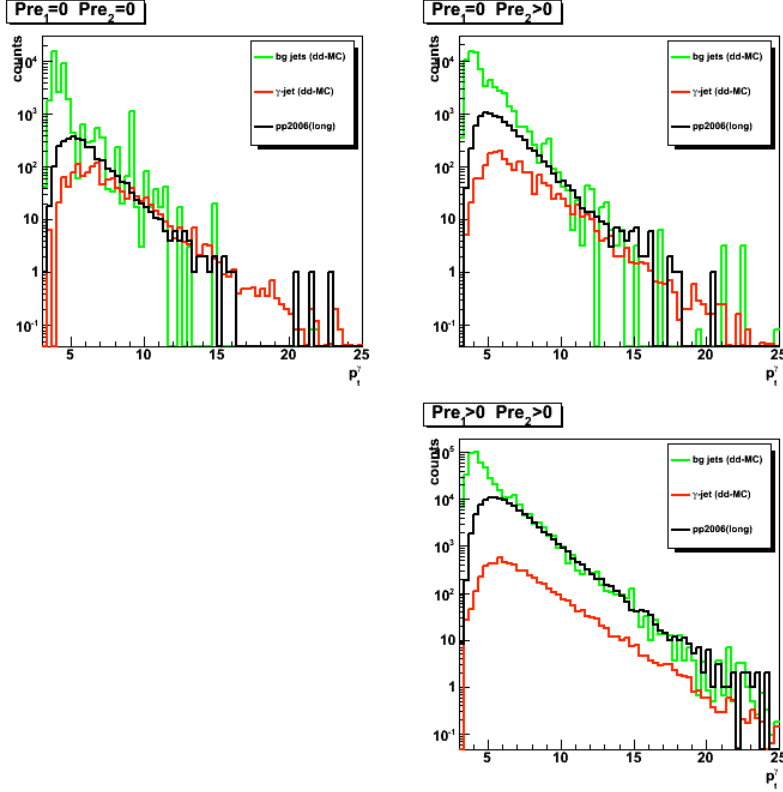


Figure 11. Candidate photon-jet yields for 2006 data compared to full detector simulations of PYTHIA generated direct photon-jet and other soft and hard QCD processes. The Monte Carlo samples are normalized to the same integrated luminosity as sampled for the data. Events with two jets are selected from a jet finder. They are checked to be back to back in azimuthal angle ϕ . Any jet in the endcap with a neutral fraction (p_T in 3×3 calorimeter tower cluster/ p_T of jets, plus tracks in an η - ϕ radius of 0.7) > 0.9 , is labeled a photon candidate and plotted above. The different panels represent different pre-shower detector conditions, indicating the point of conversion. Upper-left: vetoes on the first two layers of the calorimeter, indicating conversion after the 1st layer of lead. The upper-right panel is for a veto by the scintillator layer preceding the first Pb layer of the calorimeter and selects events that have not begun to shower prior to the calorimeter. The lower-right accepts events that have signals in both preshower layers, i.e. that have begun to shower upstream of the calorimeter.

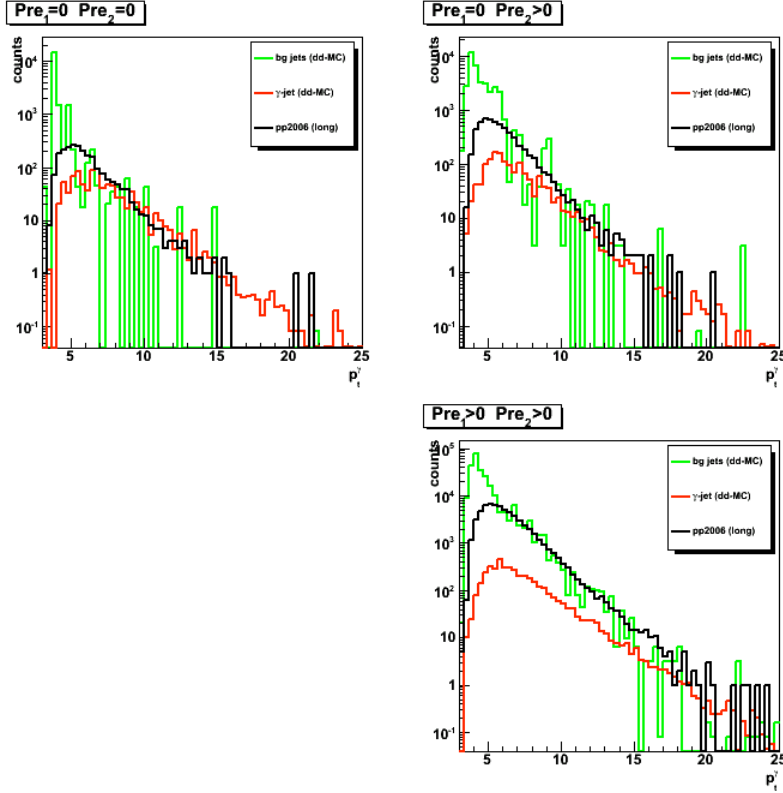


Figure 12. Candidate photon-jet yields as in Fig. 11 but with a tighter cut on the neutral fraction in a cluster. These require >0.99 in the candidate photon cluster.

In Fig. 12 a substantially stronger cut on the fraction of energy in the photon candidate compared to the isolation cone has been made. Note the substantially improved signal to background ratio. There is considerable work required to optimize isolation cuts. We are also anxious to analyze data from 2008 where the inner tracking and their substantial support services (cables etc.) were removed. This will be the configuration for a 2009 run. In the following years, the FGT will provide tracking covering the full EEMC region near the beam line before much of the intervening material. The new inner tracking will be installed with recognition of the need to limit material in this η range.

The preshower conditions provide special samples. Vetoes on the preshowers reduce the π^0/γ ratios, providing clean samples for analysis. The condition where only the 2nd preshower fires, provides a sample with a conversion probability that can be well determined. By comparing this sample to the events that do not fire the 1st preshower it is possible to make a good estimate of the π^0/γ ratio in that sample. This allows for an accurate separation of the gamma yield in the sample. We expect this method to have an advantage at lower p_T where the increasing backgrounds can be effectively suppressed by the conversion information and where the increased yields compensate for the loss in efficiency. A comparison of conversion rates for isolated gammas from identified η s to the expectation from the material in one layer between the first two preshowers is shown in the figure below.

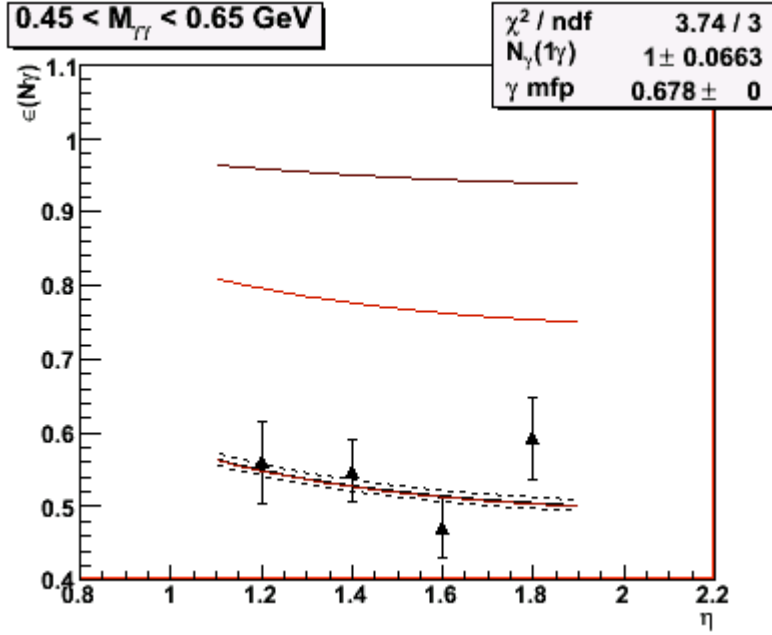


Figure 13. Conversion probability of isolated gammas from identified η s (points) plotted as a function of pseudo-rapidity and compared to a calculation based on the amount of material (one calorimeter radiator layer) intervening between the two preshower layers used to determine the conversion ratio. The upper two curves are for the probability that at least one of 2-photon and 3-photon events converts.

The calorimeters were built with shower maximum detectors (SMD) to perform shower shape analyses to help in π^0/γ discrimination based on the double separated shower of the π^0 . A major difficulty in this analysis has been the difference in observed shower shapes between Monte Carlo and data, as shown in Fig.14. This issue has been addressed by selecting a library of single-photon candidates from η decays and using those in the Monte Carlo to replace the generated shower shapes at the SMD. Continued detailed studies are underway.

It is important to note that, while the gamma jet channel is a rare process and statistically limited in the amount of luminosity we may collect in the coming 5 years, competitive measurements in this important channel could be made in the next 5 years if the efforts described above are successful in providing high efficiency and sufficiently low backgrounds. As an illustration an estimate of what could be expected from 50 pb^{-1} in a measurement with 100% efficiency and no background is shown in Fig. 15. While some inevitable loss in efficiency and backgrounds will degrade this, 50 pb^{-1} is the goal for 200 GeV in the early part of the 5 years. We expect to return to this energy for a substantial run near the end of the 5 years after central tracking has been added to both experiments and comparison pp data is needed for the heavy ion program. Better estimates of what is ultimately achievable await further results from the ongoing studies.

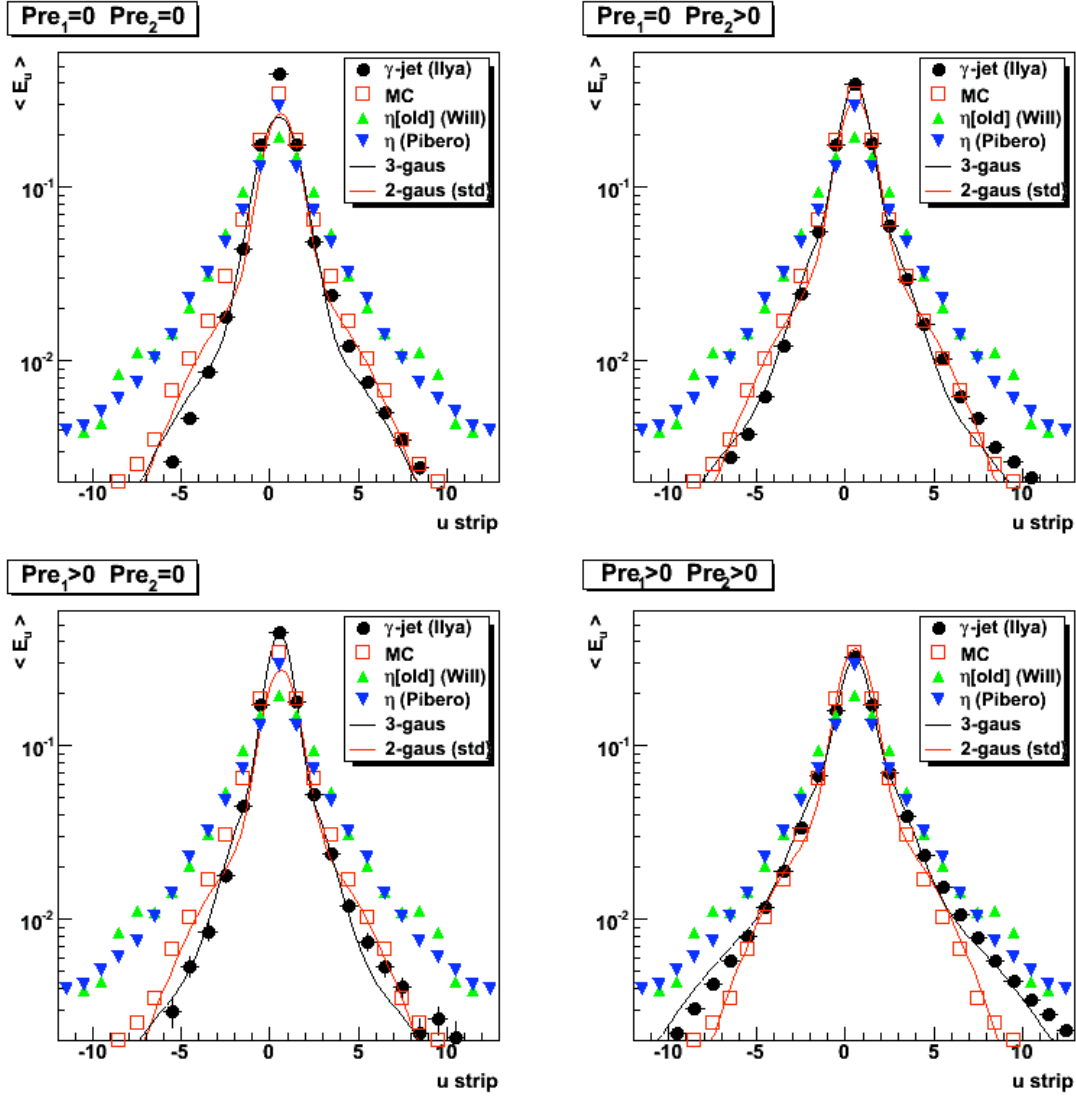


Figure 14. Single photon shower shapes. Each set of points represents the average over many events of the signal in each of 30 strips centered on the shower. The black and red points indicate full STAR detector Monte Carlo simulations. The blue and green points represent single photons isolated from identified η decays where the two photons are widely separated due to decay kinematics.

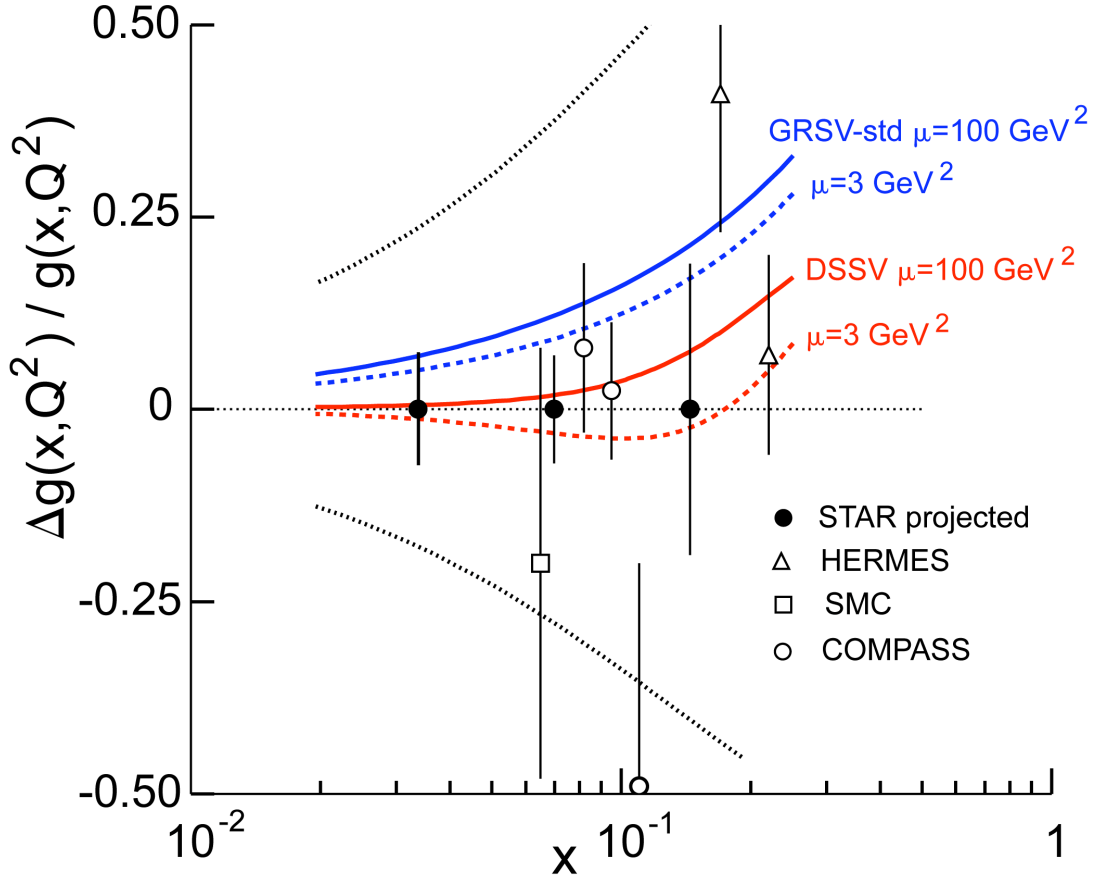


Figure 15. A_{LL} for gamma-jet correlations. The error bars represent the uncertainties we would get for an ideal experiment with 50 pb^{-1} . Only statistics in kinematics where the conversion between A_{LL} and $\Delta g/g$ can be made in a straightforward manner are included. The yield is sufficient in the coming years to make measurements with impact on the physics. An estimate of the actual luminosity required considering efficiencies and backgrounds, requires completion of the studies described above. Hermes points are from [14], COMPASS [15] and SMC [16].

Gamma-jet correlations in the far forward region

We have discussed the opportunities for measurements of photon-jet correlations in the main document, Sec. 4.2.1. STAR has recently commissioned and operated in 2008 the forward meson spectrometer (FMS), a Pb glass calorimeter that spans the pseudorapidity range $2.5 < \eta < 4.0$. Early simulations have shown that selecting a sub-range in pseudorapidity as a fiducial volume, $3.1 < \eta < 3.4$, as shown in Fig. 16, and using the rest of the calorimeter as an isolation veto, provides a suitably clean signal. This is shown in Fig. 7 of the main document. To complete the determination of the two body kinematics in order to have sensitivity to $\Delta g(x)$, requires detecting the away-side jet. Initial studies of the detection of this low energy jet with $p_T \sim 2 \text{ GeV}$ are shown in Fig. 19 of the main document. The away-side coincidence should also reduce the fragmentation

background. Rough estimates indicate that these measurements could provide important constraints on the size of $\Delta g/g$, at the few percent level. This should be possible in the region a few times $10^{-3} < x < 0.02$. Extensive work with simulations and data taken in 2008 are required to fully understand backgrounds and yields before more quantitative statements can be made.

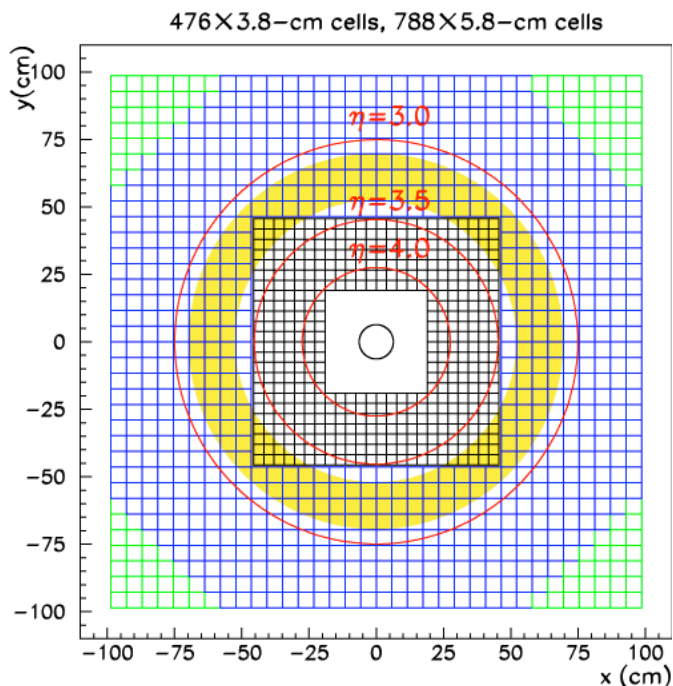


Figure 16. A schematic of the STAR forward meson spectrometer as seen from the interaction point. The Blue beam penetrates into the page at the center of the diagram. The yellow shaded area represents a conservative fiducial volume used for detection of direct γ candidates, with the remainder of the FMS used as a veto of photons arising primarily from π^0, η decays.

Heavy Flavor Measurements

Both detector collaborations are working on tracking upgrades for central and forward rapidity regions to enhance their capabilities to access heavy quark physics, especially, charm and beauty in pp and heavy ion collisions. At any given center of mass energy, the heavy quark masses set the hard scale for the event, i.e. for the reliable applicability of pQCD. When the experiments are equipped with these upgrades, heavy quarks along with the forward physics capabilities due to other upgrades will allow both experiments to make gluon polarization measurements at lower and higher x values than being pursued presently using the central barrels and 200 GeV center-of-mass operation of RHIC. These same ideas will apply for variations of the center of mass energy from 62 GeV to 500 GeV, provided sufficient integrated luminosity can be accumulated.

References

- [1] S.S. Adler et al. [PHENIX Collaboration], Phys. Rev. Lett. **93**, 202002 (2004); Phys. Rev. **D73**, 091102 (2006); A. Adare et al. [PHENIX Collaboration], Phys. Rev. **D76**, 051106(2007).
- [2] B.I. Abelev et al. [STAR Collaboration], Phys. Rev. Lett. **97**, 252001 (2006); arXiv:0710.2048 [hep-ex].
- [3] K. Boyle [PHENIX Collaboration], talk at the 2007 RHIC AGS Users' Meeting, BNL, June 2007.
- [4] M. Sarsour [STAR Collaboration], talk at the 2007 APS DNP meeting, Newport News, Virginia, Oct. 2007.
- [5] B. Jäger, A. Schäfer, M. Stratmann and W. Vogelsang, Phys. Rev. **D67**, 054005 (2003).
- [6] B. Jäger, M. Stratmann and W. Vogelsang, Phys. Rev. **D70**, 034010 (2004).
- [7] M. Glück, E. Reya, M. Stratmann and W. Vogelsang, Phys. Rev. **D63**, 094005 (2001).
- [8] T. Gehrmann and W. J. Stirling, Phys. Rev. **D53**, 6100 (1996).
- [9] E. Leader, A. V. Sidorov and D. B. Stamenov, Phys. Rev. **D75**, 074027 (2007).
- [10] M. Hirai, S. Kumano and N. Saito, Phys. Rev. **D74**, 014015 (2006).
- [11] D. de Florian, G. A. Navarro and R. Sassot, Phys. Rev. **D71**, 094018 (2005).
- [12] J. Blümlein and H. Böttcher, Nucl. Phys. **B636**, 225 (2002).
- [13] D. de Florian, R. Sassot, M. Stratmann and W. Vogelsang, arXiv:0804.0422 [hep-ph].
- [14] A. Airapetian et al. [HERMES Collaboration], Phys. Rev. Lett. **84**, 2584 (2000); P. Liebing et al. [HERMES Collaboration], arXiv:0707.3617v1 [hep-ex] .
- [15] E.S. Ageev et al., Phys. Lett. **B633**, 25 (2006) ; M. Alekseev *et al.* [COMPASS collaboration], arXiv:0802.3023v1 [hep-ex].
- [16] B. Adeva et al. [SMC Collaboration], Phys. Rev. **D70**, 012002 (2004).